Proceedings of the ASME 2018 International Mechanical Engineering Congress & Exposition
IMECE 2018
November 9-15, 2018, Pittsburgh, USA

IMECE2018-88429

AN INTEGRATED APPROACH FOR STATISTICAL MICROSCALE HOMOGENIZATION TO MACROSCOPIC DYNAMIC FRACTURE ANALYSIS

Bahador Bahmani
Mechanical, Aerospace
& Biomedical Engineering
University of Tennessee, Knoxville
Tullahoma, Tennessee, 37388
Email: bbahmani@vols.utk.edu

Ming Yang
Anand Nagarajan
Mechanical and Aerospace Engineering
The Ohio State University
Columbus, Ohio, 43210
Email: yang.3643@osu.edu
nagarajan.30@osu.edu

Philip L. Clarke
Mechanical, Aerospace
& Biomedical Engineering
University of Tennessee, Knoxville
Tullahoma, Tennessee, 37388
Email: pclarke1@utk.edu

Soheil Soghrati
Mechanical and Aerospace Engineering
Materials Science and Engineering
The Ohio State University
Columbus, Ohio, 43210
Email: soghrati.1@osu.edu

Reza Abedi
Mechanical, Aerospace
& Biomedical Engineering
University of Tennessee
Tullahoma, Tennessee, 37388
Email: rabedi@utk.edu

ABSTRACT

Maintaining material inhomogeneity and sample-to-sample variations is crucial in fracture analysis, particularly for quasi-brittle materials. We use statistical volume elements (SVEs) to homogenize elastic and fracture properties of ZrB_2-SiC, a two-phase composite often used for thermal coating. At the mesoscale, a 2D finite element mesh is generated from the microstructure using the Conforming to Interface Structured Adaptive Mesh Refinement (CISAMR), which is a non-iterative algorithm that tracks material interfaces and yields high-quality conforming meshes with adaptive operations. Analyzing the finite element results of the SVEs under three traction loadings, elastic and angle-dependent fracture strengths of SVEs are derived. The results demonstrate the statistical variation and the size effect behavior for elastic bulk modulus and fracture strengths. The homogenized fields are mapped to macroscopic material property fields that are used for fracture simulation of the reconstructed domain under a uniaxial tensile loading by the asynchronous Spacetime Discontinuous Galerkin (aSDG) method.

INTRODUCTION

Fracture and damage in materials often initiate from microstructural defects. In ductile materials energy dissipation mechanisms in the bulk such as plasticity can significantly redistribute stress field, thus reducing the effect of the most critical microstructural defects. On the other hand, due to the lack of significant bulk energy dissipation mechanisms, quasi-brittle materials are very sensitive to such defects [1,2]. Variations on crack paths under the same problem set-up [3] and ultimate strength / fracture energy uncertainties [4,5] are some of the consequences of this sensitivity. The so-called *size effect*, the decrease in the mean and variation of fracture strength as a specimen size increases, can also be explained by the random distribution of flaws.

The *explicit* models directly incorporate defects larger than certain size in the analysis. However, their application is limited to very small space and time scales due to their high computational demand. On the other hand, the *implicit* approaches only incorporate the effect of defects in an averaged, statistical,

or homogenized sense. For example, the Weibull's weakest link model [6, 7] can qualitatively explain the size effect. However, the weakest link model is not appropriate for 2D and 3D problems and phenomenological models such as the Weibull model lack a direction connection to material microstructure.

Homogenization approaches address the aforementioned concerns, in that they derive the macroscopic properties of a material by solving an underlying problem in a *Volume Element* (VE). Beyond numerous works in elastic regime, [8–11] have used homogenization to calibrate certain fracture models. A *Representative Volume Element* (RVE) refers to a VE that is appreciably larger than the microscale features yet smaller than the overall domain dimensions, so that the assignment of VE homogenized values to a macroscopic continuum model is well justified [12]. Because of the large size of RVEs and the practical convergence of a homogenized property to a unique value, the spatial inhomogeneity and sample to sample variation are lost when RVEs are used. On the other hand, *Statistical Volume Elements* (SVEs) are small enough to maintain material inhomogeneity and statistical variation among different realizations. The SVEs are used for modeling statistical elastic [13–15] and fracture [16] responses. For a more detailed overview of RVEs and SVEs, the reader is referred to [12, 17].

The authors have shown that incorporating statistical variations and inhomogeneity of fracture strength is critical in problems that lack macroscopic stress concentration points, *e.g.,* fracture under dynamic compressive loading [18] and fragmentation studies [19]. However, due to the use of the Weibull model there was no direct connection to material microstructure. We employed SVEs containing microcracks [20, 21] and circular inclusions [22]. However, first the construction of microcracks or inclusions was not based on real material microstructures; second, very simplified fracture models were used at the microscale, in that microcracks did not interact in the former and could only nucleate at inclusion-matrix interfaces in the latter works.

One approach to overcome the challenges associated with the realistic modeling of material microstructures is to implement an appropriate reconstruction algorithm, such as descriptor-based algorithms [23–25]. In such algorithms, an optimization phase is often utilized to replicate a set of statistical descriptor functions such as the size distribution and spatial arrangement of particles in the microstructure [26–28]. Several correlation function-based algorithms [29, 30] have also been introduced for reconstructing material microstructures using various techniques, such as those relying on random sequential adsorption [31–33] and Voronoi tessellation [34–36]. Simulating the desired spatial arrangement of inclusions in such reconstruction techniques often requires implementing computationally demanding algorithms such as the Monte-Carlo method [37, 38] and pixel switching [39, 40]. Recently, Yang et. al [25] have introduced a new animation-inspired algorithm for the virtual reconstruction of various heterogeneous material microstructures. In addition to a low computational cost and the ability to handle arbitrary-shaped inclusions, this algorithm provides an explicit representation of materials interfaces using Non-Uniform Rational B-Splines (NURBS) [41], which highly facilitates subsequent finite element (FE) analyses.

Creating high-quality conforming meshes with proper element shapes and aspect ratios is another major challenge toward the FE modeling of problems with complex morphologies [42]. Among popular mesh generation techniques for the treatment of such problems we can mention the Delaunay triangulation [43], advancing front [44, 45], quadtree/octree-based techniques [46, 47], and the marching cubes [48, 49]. However, the iterative smoothing/optimization process involved in such algorithms for improving element aspect ratios in problems with intricate geometries could be computationally demanding and even fail to converge in some case scenarios. FE-based enriched methods such as CutFEM [50], eXtended FEM (XFEM) [51,52], and the Hierarchical Interface-enriched FEM (HIFEM) [53, 54] have also been utilized to make the simulation process independent of the underlying mesh structure. However, there are challenges associated with the implementation of such algorithms for modeling interface problems, such as the ill-conditioning of the stiffness matrix and a loss of accuracy in recovery of the gradient field along material interfaces, where the latter could considerably deteriorate the fidelity in predicting stress concentrations in multiphase problems.

In order to address the limitations outlined above in the implementation of mesh generation algorithms and enriched FE-based techniques, Soghrati et al. [55, 56] have recently introduced a non-iterative meshing algorithm that preserves the most salient advantages of both approaches. Similar to the former class of methods and regardless of the complexity of geometry, CISAMR enables the use of a simple structured mesh for discretizing the domain. However, rather than implementing enrichment functions to capture the discontinuous phenomena, it can non-iteratively transform this initial structured mesh into a high-quality conforming mesh using customized versions of *h*-adaptivity, *r*-adaptivity, and sub-triangulation algorithms [55]. The CISAMR algorithm for modeling 3D problems is presented in [57] and has previously been implemented for modeling a variety of materials with complex geometries, including fiber reinforced composites [58] and DNA-origami nanostructures [59].

In this manuscript, the microstructure reconstruction algorithm presented in [25] is employed to build a large microstructural model of a ZrB_2-SiC particulate composite. CISAMR is then employed to automatically build FE models and simulate the micromechanical behavior of hundreds of SVEs of this material with various sizes and under the traction boundary condition. In addition, detailed FE analyses are performed at the microscale and unlike [22] fracture can nucleate in the matrix or inclusion phases or the interfaces between the two.

The macroscopic fracture simulations are performed by the

asynchronous discontinuous Galerkin (aSDG) method [60]. The convergence of the crack path for a deterministic problem is demonstated in [19]. For stochastic models, our preliminary results demonstrate the objectivity of various macroscopic measures such as fracture energy and ultimate load for the tensile fracture problem presented in the numerical results section. These features ensure the accuracy of macroscopic fracture simulations.

FORMULATION

Microstructure reconstruction and meshing

Figure 1 illustrates a 800 μm $\times$ 800 μm RVE of the ZrB_2-SiC particulate composite with a volume fraction of $V_f = 20\%$ that will be analyzed in this work. The NURBS-based reconstruction algorithm presented in [25] is employed to synthesize this microstructural model, which consists of 6654 embedded particles. For this purpose, the scanning electron microscope (SEM) images provided in [61] are processed and segmented to extract morphologies of a representative set of particles, which are parameterized in terms of NURBS functions and stored in a shape library. The imaging data are also used to determine the size distribution and spatial arrangement of particles, which are statistically characterized using a normal distribution function and a two-point correlation function, respectively. A hierarchical bounding box based packing algorithm [25] is then employed to initially pack more than 20,000 particles in the domain. We then implement a GA-based optimization framework to selectively eliminate some of this particles to simulate the target two-point correlation function, resulting in the non-uniform spatial arrangement of particles shown in Fig. 1.

The homogenization-based fracture analysis presented in this manuscript is conducted based on the FE simulation of micromechanical behavior of hundreds of SVEs of the ZrB_2-SiC RVE depicted in Fig. 1. This in turn requires the automated construction of appropriate conforming meshes for each heterogeneous SVE, which is accomplished using CISAMR [55]. For example, 4,096 distinct FE models are created for non-overlapping SVEs with the length of $L = 12.5$ μm. All these meshes are created by starting with an initial structured mesh with the element size of $h = 1$ μm, which is overlapped on each SVE of the original microstructural model. The CISAMR non-iterative algorithm then transforms this background mesh into a high-quality conforming mesh by applying 2 levels of refinement along material interfaces. A small portion of one of the resulting meshes generated using this algorithm is depicted in Fig. 2.

Loading of SVEs

To calculate elastic stiffness tensor and angle-dependent fracture strength, we load the SVEs with traction boundary condition. The average macroscopic stress tensor, in Voight notation,

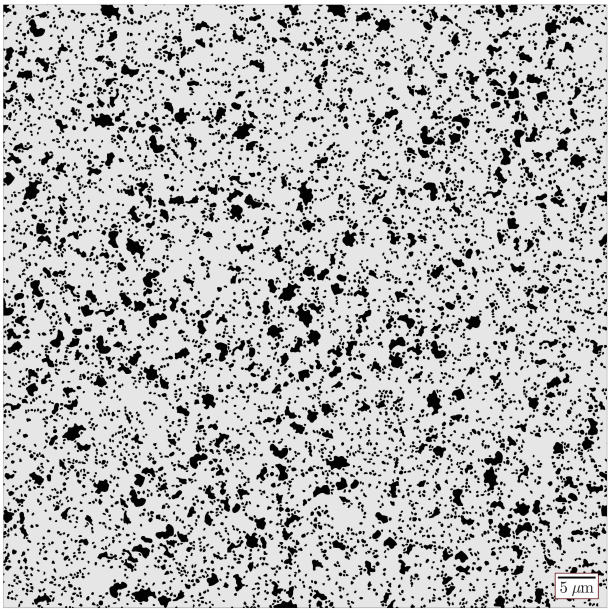

FIGURE 1. VIRTUALLY RECONSTRUCTRED ZrB_2-SiC RVE ($V_f = 20\%$).

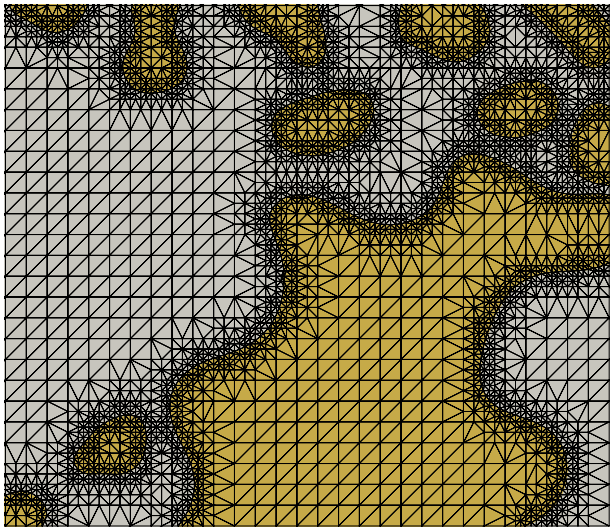

FIGURE 2. PORTION OF THE CONFORMING MESH GENERATED USING CISAMR FOR DISCRETIZING ONE OF HE SVES OF THE MICROSTRUCTURAL MODEL SHOWN IN FIGURE 1.

is denoted by,

$$\bar{\mathbf{S}} = [\bar{S}_{xx}, \bar{S}_{yy}, \bar{S}_{xy}]^{\intercal} \tag{1}$$

where $\intercal$ is the transpose operator. For a homogenization analysis with stress boundary conditions, three load cases are considered

with tractions on the boundaries that correspond to nonzero $\bar{S}_{xx}$, $\bar{S}_{yy}$, and $\bar{S}_{xy}$, respectively. Figure 3 shows the microscopic σ_{11} distribution inside an SVE, due to the macroscopic traction loading with nonzero $\bar{S}_{xx}$ value. By computing the average Voight strains for each of these loadings, the 3×3 stiffness matrix $\mathbf{C}$ is computed for each SVE. The bulk modulus κ is then computed from $\mathbf{C}$ by considering a hydrostatic pressure loading. As will be discussed next, microscopic stresses in the matrix and inclusion and at the interface between the two are used to derive angle-dependent fracture strengths. Often stress concentration points around matrix and inclusion interfaces, as those shown in Fig. 3, are the sites that determine fracture

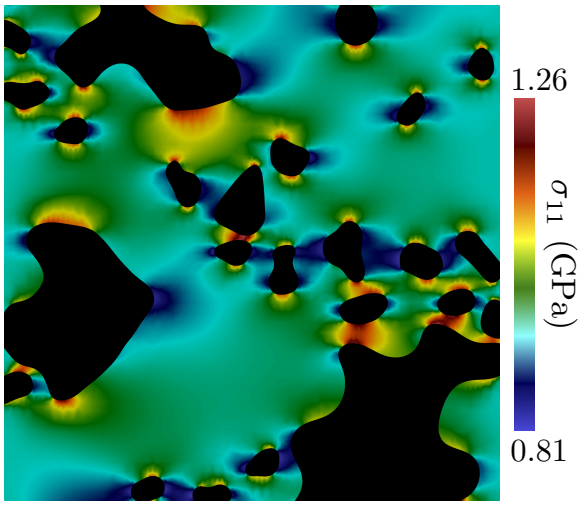

FIGURE 3. FE APPROXIMATION OF σ_{11} IN THE MATRIX OF ONE OF THE SVES WIH $L = 50$ μm USING THE TRACTION BOUNDARY CONDITION SIMULATING A MACROSCOPIC NORMAL STRESS APPLIED IN THE x-DIRECTION.

Failure criterion

Three different failure modes are considered for the composite. The matrix and inclusions are isotropic elastic media, whose failure are characterized by an isotropic Mohr-Coulomb model. The microscopic uniaxial/hydrostatic tensile and uniaxial compressive strengths are denoted by s_n^α, s_t^α, respectively, where $\alpha \in \{M, I\}$ corresponds to "Matrix" and "Inclusion" phases. The third failure mode corresponds to the interface between the matrix and inclusion, where it is assumed that fracture occurs when tensile stress at any point of the interfaces in an SVE reaches the interface strength s_n^i, where i refers to the interface phase.

The macroscopic tensile and shear strengths are obtained by finding the average stresses that correspond to macroscopic tensile and shear loadings at an arbitrary angle θ. Figure 4 shows

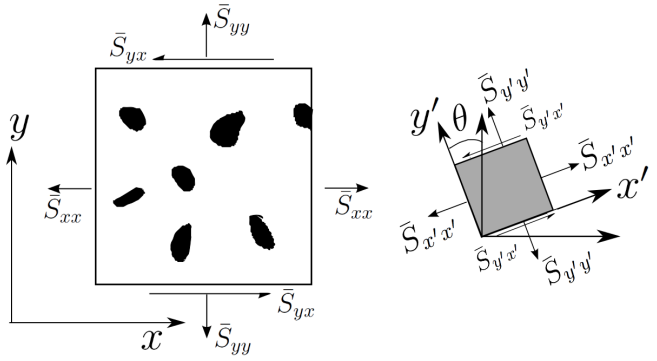

FIGURE 4. SCHEMATIC OF AN SVE AND THE x', y' AXES FOR FAR-FIELD LOADING RELATIVE TO GLOBAL x, y AXES.

the global $\{x, y\}$ and local $\{x', y'\}$ coordinate systems used for applying the macroscopic BCs and computing strengths for angle θ, respectively. For the rotated coordinate system $\{x', y'\}$, the only nonzero values of $\bar{S}_{y'y'} = 1$ and $\bar{S}_{y'x'} = 1$ correspond to pure tensile and shear loadings at the angle θ. The Mohr circle is used to find the linear superposition of components of $\bar{\mathbf{S}}$ in Eqn. (1) that generate such macroscopic tensile and shear loadings [62]. The microscopic stresses in the matrix, inclusion, and interface are computed by the same superposition of their corresponding values from the three traction loadings in Eqn. (1).

The macroscopic tensile strength at angle θ, $\tilde{s}_n(\theta)$, is obtained by finding the load factor $s = \tilde{s}_n(\theta)$ relative to the solution for $\bar{S}_{y'y'} = 1$, such that the most critical point in the matrix, inclusion, or the interfaces in an SVE fails. The shear strength $\tilde{s}_t(\theta)$ is obtained by the same process, where the load factor is computed relative to the solution for $\bar{S}_{y'x'} = 1$. The association of the strength of the SVE with the load at which the overall failure of SVE initiates is motivated by [63, 64] where it is shown that under quasi-static and low to medium loading rates, ultimate strength of a volume element is very close to the stress level at which failure initiates.

NUMERICAL RESULTS

Statistical analysis of SVEs

For the analysis ZrB_2-SiC SVEs the following material properties are used for the ZrB_2 matrix: Young's modulus $E^M = 524$ GPa, Poisson's ratio $\nu^M = 0.2$, tensile strength $s_n^M = 381$ MPa, and compressive strength $s_c^M = 2.5$ GPa. The properties of inclusion phase SiC are: Young's modulus $E^I = 415$ GPa, Poisson's ratio $\nu^I = 0.2$, tensile strength $s_n^I = 359$ MPa, and compressive strength $s_c^I = 2.1$ GPa. The volume fraction of SiC in an 800 μm $\times$ 800 μm RVE is 20%. The interface tensile strength is taken to be 80% of the minimum of the tensile strengths of matrix and inclusion phases, which is a reasonable assumption for

composites of this type.

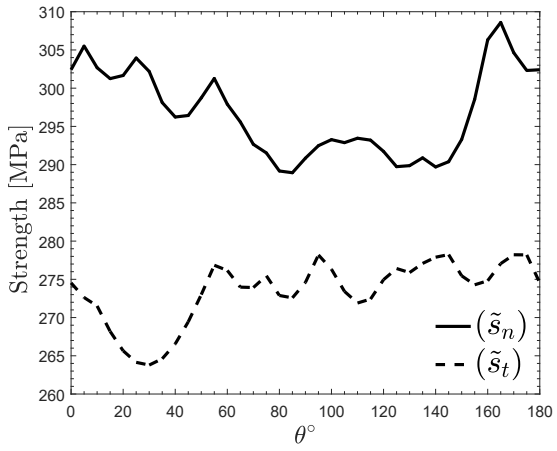

FIGURE 5. ANGULAR VARIATION OF NORMAL STRENGTH $\tilde{s}_n(\theta)$ AND SHEAR STRENGTH $\tilde{s}_t(\theta)$ FOR ONE 12.5 μm $\times$ 12.5 μm SVE.

The angular variation of normal fracture strengths $\tilde{s}_n(\theta)$ and shear strength $\tilde{s}_t(\theta)$ are shown for a sample 12.5 μm $\times$ 12.5 μm SVE. First, it is observed that the tensile strength is higher for all angles of loading. This is expected as for both the matrix and inclusion phases, the tensile strength is higher than the shear strength. Second, the angular variation of strengths over angle is smaller than about 7% of their corresponding mean angular values. That is, even at such small SVE sizes, the fracture strength response is not highly anisotropic. As a result, in the following the conservative minimum strengths over all angles of loading, that is $\min(\tilde{s}_n)$ and $\min(\tilde{s}_t)$, are used to characterize the strengths of an SVE.

To investigate the SVE to SVE variation of fracture strength, the *probability density function* (PDF) of $\min(\tilde{s}_n)$ is shown in Fig. 6. First, it is observed that both the strengths with the highest probability and the mean values decrease as the SVE size increases. Second, for the smallest SVE size (12.5 μm $\times$ 12.5 μm), a secondary bump appears in the PDF. The strengths around this bump are close to the tensile strength of the matrix s_n^M. The appearance of this bump is similar to the transition of the PDF of elastic stiffness from a bimodal to a hump-shaped PDF in [65], where at very small sizes we can encounter SVEs only comprised of the matrix material.

The PDF for the minimum shear strength $\min(\tilde{s}_t)$ is shown in Fig. 7. A similar trend to $\min(\tilde{s}_t)$ is observed here with the difference that shear strengths are smaller than tensile strengths. This is expected as for both phases, the same holds true for microscopic strength values.

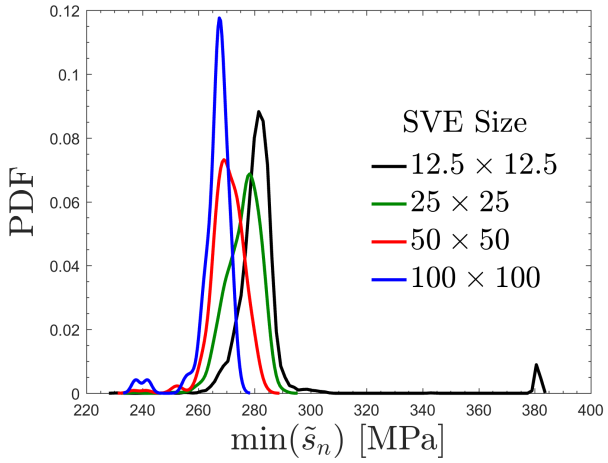

FIGURE 6. PDF OF MINIMUM TENSILE STRENGTH $\min(\tilde{s}_n)$, FOR DIFFERENT SVE SIZES.

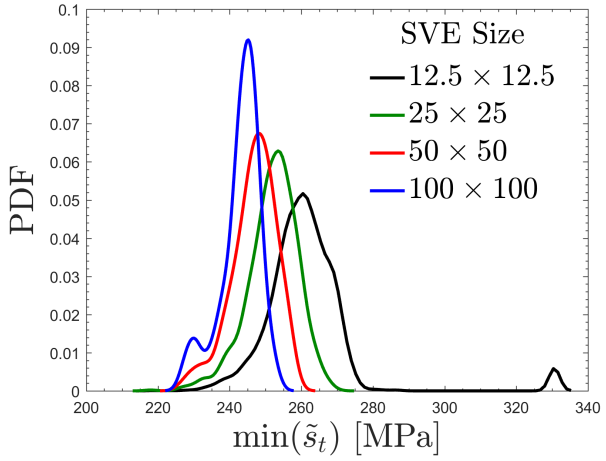

FIGURE 7. PDF OF MINIMUM SHEAR STRENGTH $\min(\tilde{s}_n)$, FOR DIFFERENT SVE SIZES.

To better understand the effect of the size of SVE on its properties, a size effect plot of the bulk modulus is presented in Fig. 8. The mean value and min/max values of the bulk modulus are shown by solid and dashed lines, respectively. For larger SVEs the variation of its bulk modulus decreases. As the SVE size increases, the variations of κ are expected to tend to zero and its value to converge to the RVE limit bulk modulus. Another interesting observation is having very little variation in the mean value of κ across different SVE sizes. We use this feature to choose a homogeneous bulk modulus for macroscopic fracture simulations reported below.

The size effect for the minimum tensile strength (over all angles), $\min(\tilde{s}_n)$, is shown in Fig. 9. This figure demonstrates

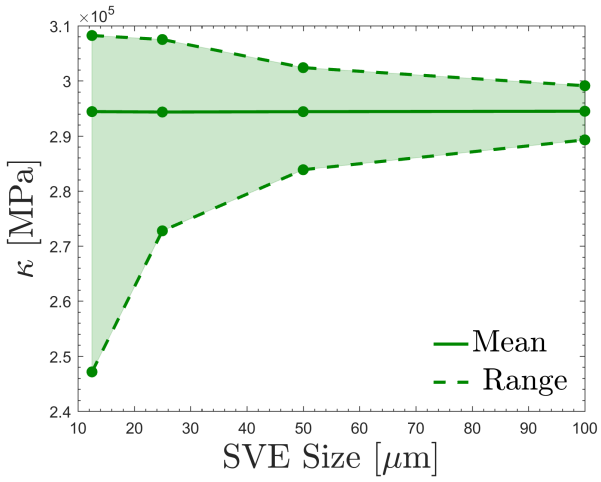

FIGURE 8. SIZE EFFECT PLOT FOR BULK MODULUS κ. THE MEAN AND RANGE (MINIMUM AND MAXIMUM) ARE SHOWN BY SOLID AND DASHED LINES.

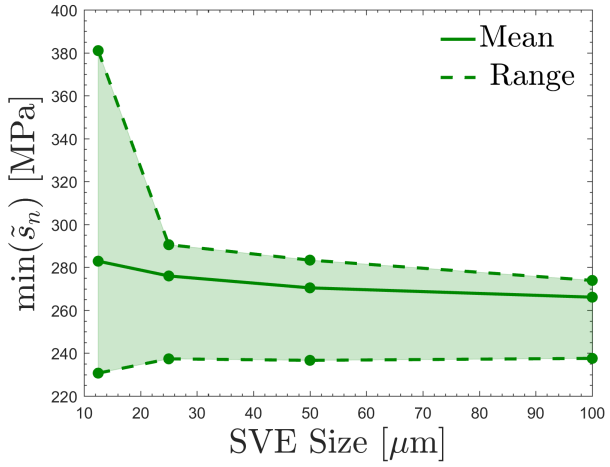

FIGURE 9. SIZE EFFECT PLOT FOR MINIMUM TENSILE STRENGTH $\min(\tilde{s}_n)$.

the typical *size effect* response expected for fracture strength, in that the mean of fracture strength decreases as the SVE size increases; see for example [66]. At the same time, the variation of fracture strength significantly decreases as the SVE size increases. The decrease in the mean value is explained by the fact that as the SVE size increases there is a higher likelihood for having more critical stress concentration points within an SVE. The decrease of variation is contributed to the higher population of stress concentration points within SVEs as their size increases.

Macroscopic fracture analysis

For the macroscopic fracture analysis, the 800 μm $\times$ 800 μm RVE is subdivided by $32 \times 32 = 1024$ 25 μm $\times$ 25 μm SVEs. For each SVE the conservative tensile strength $\min(\tilde{s}_n)$ is used in the material input mesh; the values between the grid points are linearly interpolated. For elastic properties, a homogeneous and isotropic material with a bulk modulus corresponding to the mean value shown in Fig. 8 is used. The use of an isotropic material is motivated by the fact that various measures of material anisotropy, *cf. e.g.,* [67], classify the material with less than about 3% of anisotropy (results not provided for brevity). The use of homogeneous elastic properties is motivated by the fact that the inhomogeneous nucleation and propagation of cracks due to variations of fracture strengths play a more critical role than stress redistribution due to variations of bulk modulus for the simple tensile test considered herein.

For the analysis of macroscopic elastodynamic problem the the asynchronous spacetime discontinuous Galerkin (aSDG) method [60] is used. The minimum tensile and shear strength values, $\min(\tilde{s}_n)$ and $\min(\tilde{s}_t)$, are used in the definition of a scalar effective traction [68] that in our formulation drives crack nucleation, propagation, and damage evolution on fracture interfaces [19]. Due to the dynamic loading of the domain and brittle nature of fracture, complex fracture patterns are expected for this problem. As a result, we use general spacetime mesh adaptive operations [69], dual error indicators in the bulk and on fracture surfaces [70] to ensure the accuracy of the solution. Moreover, the fracture specific mesh adaptive operations [71] accommodate crack propagation in any desired direction. The latter is critical in capturing realistic fracture patterns.

Figure 10 shows the results for a simple tensile loading on the RVE where the left boundary is fixed and the right boundary is pulled with the normal velocity that ramps up from zero to its terminal value $\bar{v} = 4.5$ m/s in 35 ns. The value of $\bar{v}$ is chosen such that the corresponding tensile loading carried by the wave inside the domain is slightly lower than the mean value of $\min(\tilde{s}_n)$ over the RVE. If the fracture strength was a uniform value, the entire domain would have failed along vertical lines as the wave propagated inward. However, the inhomogeneity of fracture strength results in the nucleation of cracks from the weak points of the domain and the type of fracture pattern observed in the figure. For example, in Fig. 10(b) a few cracks are nucleated behind the wave front and stress field is relaxed around them. Figure 10(c) shows the instant where the elastic wave reaches the far left boundary, having created the main crack nucleation sites behind. The final fracture pattern is shown in Fig. 10(d). In all the figures the strain energy density is shown on the deformed geometry, where blue to red colors correspond to zero to high values.

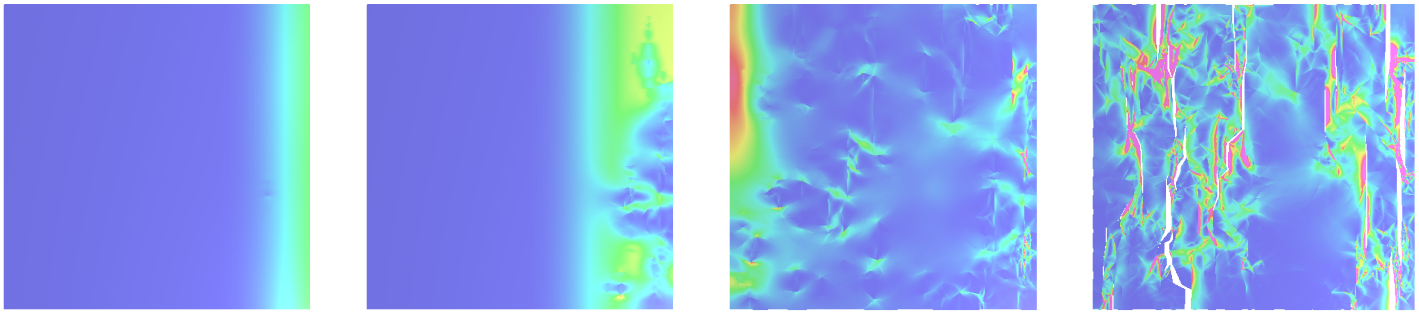

(a) TIME $t = 26$ ns. (b) TIME $t = 40$ ns. (c) TIME $t = 96$ ns. (d) TIME $t = 960$ ns.

FIGURE 10. SOLUTION VISUALIZATION FOR A TENSILE LOADING ON A DOMAIN WITH SVE-HOMOGENIZED FRACTURE STRENGTH.

CONCLUSIONS

We used the CISAMR method to generate a volume element based on realistic distribution of inclusions in a ZrB_2-SiC composite. We subdivided this volume element to SVEs of different sizes and derived their elastic properties by applying traction boundary conditions. Furthermore, by the superposition of the results corresponding to these distinct boundary conditions, we derived the angle-dependent tensile and shear fracture strengths of the SVEs.

The analysis of the SVEs revealed interesting results. First, the variation of both bulk modulus and fracture strengths decreased when larger SVEs were used. Second, the mean values of fracture strengths mildly decreased by the increase of the SVE size. Third, the mean value of the bulk modulus was quite stable across all SVE sizes. We used the SVE-based homogenized fracture strengths in a macroscopic fracture simulation where the original volume element was subject to a dynamic tensile loading; as expected, cracks only nucleated from the weak sites of the material and the inhomogeneity prevented simultaneous failure of material as tensile wave front passed through the domain. Future work will further study the correlation of elastic and fracture properties and the effect of the length at which homogenization occurs, *i.e.,* the SVE size, on macroscopic fracture measures such as ultimate load and fracture energy.

ACKNOWLEDGMENT

Abedi, Bahmani, and Clarke acknowledge partial support for this work via the U.S. National Science Foundation (NSF), CMMI - Mechanics of Materials and Structures (MoMS) program grant number 1538332. Soghrati and Yang acknowledge the funding from the National Science Foundation under Grant No. 1608058, as the support from the Ohio State University Simulation Innovation and Modeling Center (SIMCenter).

REFERENCES

[1] Rinaldi, A., Krajcinovic, D., and Mastilovic, S., 2007. "Statistical damage mechanics and extreme value theory". *International Journal of Damage Mechanics,* ***16***(1), pp. 57–76.

[2] Genet, M., Couegnat, G., Tomsia, A., and Ritchie, R., 2014. "Scaling strength distributions in quasi-brittle materials from micro- to macro-scales: A computational approach to modeling nature-inspired structural ceramics". *Journal of the Mechanics and Physics of Solids,* ***68***(1), pp. 93–106.

[3] Al-Ostaz, A., and Jasiuk, I., 1997. "Crack initiation and propagation in materials with randomly distributed holes". *Engineering Fracture Mechanics,* ***58***(5-6), pp. 395–420.

[4] Kozicki, J., and Tejchman, J., 2007. "Effect of aggregate structure on fracture process in concrete using 2D lattice model". *Archives of Mechanics,* ***59***(4-5), pp. 365–84.

[5] Yin, X., Chen, W., To, A., McVeigh, C., and Liu, W. K., 2008. "Statistical volume element method for predicting microstructure–constitutive property relations". *Computer methods in applied mechanics and engineering,* ***197***(43-44), pp. 3516–29.

[6] Weibull, W., 1939. "A statistical theory of the strength of materials". *R. Swed. Inst. Eng. Res.*, p. Res. 151.

[7] Weibull, W., 1951. "A statistical distribution function of wide applicability". *Journal of Applied Mechanics,* ***18***, pp. 293–297.

[8] Taylor, L. M., Chen, E.-P., and Kuszmaul, J. S., 1986. "Microcrack-induced damage accumulation in brittle rock under dynamic loading". *Computer Methods in Applied Mechanics and Engineering,* ***55***(3), pp. 301 – 320.

[9] Homand-Etienne, F., Hoxha, D., and Shao, J., 1998. "A continuum damage constitutive law for brittle rocks". *Computers and Geotechnics,* ***22***(2), pp. 135–151.

[10] Shao, J., and Rudnicki, J., 2000. "A microcrack-based continuous damage model for brittle geomaterials". *Mechanics of Materials,* ***32***(10), pp. 607–619.

[11] Lu, Y., Elsworth, D., and Wang, L., 2013. "Microcrack-based coupled damage and flow modeling of fracturing evolution in permeable brittle rocks". *Computers and Geotechnics,* ***49***, pp. 226–44.

[12] Ostoja-Starzewski, M., 2002. "Microstructural randomness versus representative volume element in thermomechanics". *Journal of Applied Mechanics-Transactions of the ASME,* ***69***(1), pp. 25–35.

[13] Baxter, S. C., and Graham, L. L., 2000. "Characterization of random composites using moving-window technique". *Journal of Engineering Mechanics,* ***126***(4), pp. 389–397.

[14] Tregger, N., Corr, D., Graham-Brady, L., and Shah, S., 2006. "Modeling the effect of mesoscale randomness on concrete fracture". *Probabilistic Engineering Mechanics,* ***21***(3), pp. 217–225.

[15] Segurado, J., and LLorca, J., 2006. "Computational micromechanics of composites: The effect of particle spatial distribution". *Mechanics of Materials,* ***38***(8), pp. 873–883.

[16] Koyama, T., and Jing, L., 2007. "Effects of model scale and particle size on micro-mechanical properties and failure processes of rocks—a particle mechanics approach". *Engineering Analysis with Boundary Elements,* ***31***(5), pp. 458–472.

[17] Ostoja-Starzewski, M., 2006. "Material spatial randomness: From statistical to representative volume element". *Probabilistic Engineering Mechanics,* ***21***(2), pp. 112 – 132.

[18] Abedi, R., Haber, R., and Elbanna, A., 2017. "Mixed-mode dynamic crack propagation in rocks with contact-separation mode transitions". In Proceeding: 51th US Rock Mechanics/Geomechanics Symposium. ARMA 17-0679.

[19] Abedi, R., Haber, R. B., and Clarke, P. L., 2017. "Effect of random defects on dynamic fracture in quasi-brittle materials". *International Journal of Fracture,* ***208***(1-2), pp. 241–268.

[20] Clarke, P., and Abedi, R., 2017. "Fracture modeling of rocks based on random field generation and simulation of inhomogeneous domains". In Proceeding: 51th US Rock Mechanics/Geomechanics Symposium. ARMA 17-0643.

[21] Clarke, P., Abedi, R., Bahmani, B., Acton, K., and Baxter, S., 2017. "Effect of the spatial inhomogeneity of fracture strength on fracture pattern for quasi-brittle materials". In Proceedings of ASME 2017 International Mechanical Engineering Congress & Exposition IMECE 2017, p. V009T12A045. IMECE2017-71515.

[22] Acton, K., Baxter, S., Bahmani, B., Clarke, P., and Abedi, R., November 3-9, 2017. "Mesoscale models characterizing material property fields used as a basis for predicting fracture patterns in quasi-brittle materials". In Proceedings of ASME 2017 International Mechanical Engineering Congress & Exposition IMECE 2017, pp. V009T12A061, 6 pages. IMECE2017-71500.

[23] Xu, H., Dikin, D. A., Burkhart, C., and Chen, W., 2014. "Descriptor-based methodology for statistical characterization and 3d reconstruction of microstructural materials". *Computational Materials Science,* ***85***, pp. 206–216.

[24] Xu, H., Liu, R., Choudhary, A., and Chen, W., 2015. "A machine learning-based design representation method for designing heterogeneous microstructures". *Journal of Mechanical Design,* ***137***(5), p. 051403.

[25] Yang, M., Nagarajan, A., Liang, B., and Soghrati, S., 2018. "New algorithms for virtual reconstruction of heterogeneous microstructures". *Computer Methods in Applied Mechanics and Engineering,* ***338***, pp. 275–298.

[26] Kumar, N. C., Matouš, K., and Geubelle, P. H., 2008. "Reconstruction of periodic unit cells of multimodal random particulate composites using genetic algorithms". *Computational materials science,* ***42***(2), pp. 352–367.

[27] Liu, X., and Shapiro, V., 2015. "Random heterogeneous materials via texture synthesis". *Computational Materials Science,* ***99***, pp. 177–189.

[28] Matouš, K., Lepš, M., Zeman, J., and Šejnoha, M., 2000. "Applying genetic algorithms to selected topics commonly encountered in engineering practice". *Computer methods in applied mechanics and engineering,* ***190***(13), pp. 1629–1650.

[29] Torquato, S., 2013. *Random heterogeneous materials: microstructure and macroscopic properties*, Vol. 16. Springer Science & Business Media.

[30] Sun, Y., Cecen, A., Gibbs, J. W., Kalidindi, S. R., and Voorhees, P. W., 2017. "Analytics on large microstructure datasets using two-point spatial correlations: Coarsening of dendritic structures". *Acta Materialia,* ***132***, pp. 374 – 388.

[31] Ayyar, A., Crawford, G., Williams, J., and Chawla, N., 2008. "Numerical simulation of the effect of particle spatial distribution and strength on tensile behavior of particle reinforced composites". *Computational Materials Science,* ***44***(2), pp. 496–506.

[32] Yu, M., Zhu, P., and Ma, Y., 2013. "Effects of particle clustering on the tensile properties and failure mechanisms of hollow spheres filled syntactic foams: A numerical investigation by microstructure based modeling". *Materials & Design,* ***47***, pp. 80–89.

[33] Soghrati, S., and Liang, B., 2016. "Automated analysis of microstructural effects on the failure response of heterogeneous adhesives". *International Journal of Solids and Structures,* ***81***, pp. 250–261.

[34] Swaminathan, S., Ghosh, S., and Pagano, N., 2006. "Statistically equivalent representative volume elements for unidirectional composite microstructures: Part i-without damage". *Journal of Composite Materials,* ***40***(7), pp. 583–604.

[35] Fritzen, F., and Böhlke, T., 2011. "Periodic three-dimensional mesh generation for particle reinforced composites with application to metal matrix composites". *Inter-*

national Journal of Solids and Structures, ***48***(5), pp. 706–718.

[36] Altschuh, P., Yabansu, Y. C., Hötzer, J., Selzer, M., Nestler, B., and Kalidindi, S. R., 2017. "Data science approaches for microstructure quantification and feature identification in porous membranes". *Journal of Membrane Science,* ***540***, pp. 88 – 97.

[37] Baniassadi, M., Mortazavi, B., Hamedani, H. A., Garmestani, H., Ahzi, S., Fathi-Torbaghan, M., Ruch, D., and Khaleel, M., 2012. "Three-dimensional reconstruction and homogenization of heterogeneous materials using statistical correlation functions and fem". *Computational Materials Science,* ***51***(1), pp. 372–379.

[38] Bhaduri, A., He, Y., Shields, M. D., Graham-Brady, L., and Kirby, R. M., 2017. "Stochastic collocation approach with adaptive mesh refinement for parametric uncertainty analysis". *ArXiv e-prints*.

[39] Kumar, H., Briant, C., and Curtin, W., 2006. "Using microstructure reconstruction to model mechanical behavior in complex microstructures". *Mechanics of Materials,* ***38***(8), pp. 818–832.

[40] Liu, Y., Greene, M. S., Chen, W., Dikin, D. A., and Liu, W. K., 2013. "Computational microstructure characterization and reconstruction for stochastic multiscale material design". *Computer-Aided Design,* ***45***(1), pp. 65–76.

[41] Piegl, L., and Tiller, W., 2012. *The NURBS book*. Springer Science & Business Media.

[42] Geuzaine, C., and Remacle, J. F., 2009. "Gmsh: A 3-D finite element mesh generator with built-in pre-and post-processing facilities". *International Journal for Numerical Methods in Engineering,* ***79***(11), pp. 1309–1331.

[43] Shewchuk, J. R., 2002. "Delaunay refinement algorithms for triangular mesh generation". *Computational Geometry,* ***22***(1), pp. 21–74.

[44] Lo, S. H., 1985. "A new mesh generation scheme for arbitrary planar domains". *International Journal for Numerical Methods in Engineering,* ***21***(8), pp. 1403–1426.

[45] Schöberl, J., 1997. "NETGEN An advancing front 2D/3D-mesh generator based on abstract rules". *Computing and Visualization in Science,* ***1***(1), pp. 41–52.

[46] Baehmann, P. L., Wittchen, S. L., Shephard, M. S., Grice, K. R., and Yerry, M. A., 1987. "Robust, geometrically based, automatic two-dimensional mesh generation". *International Journal for Numerical Methods in Engineering,* ***24***(6), pp. 1043–1078.

[47] Shephard, M. S., and Georges, M. K., 1991. "Automatic three-dimensional mesh generation by the finite Octree technique". *International Journal for Numerical Methods in Engineering,* ***32***(4), pp. 709–749.

[48] Zhang, Y., Hughes, T. J., and Bajaj, C. L., 2010. "An automatic 3d mesh generation method for domains with multiple materials". *Computer methods in applied mechanics and engineering,* ***199***(5), pp. 405–415.

[49] Liang, X. H., and Zhang, Y. J., 2014. "An Octree-based dual contouring method for triangular and tetrahedral mesh generation with guaranteed angle range". *Engineering with Computers,* ***30***(2), pp. 211–222.

[50] Burman, E., Claus, S., Hansbo, P., Larson, M. G., and Massing, A., 2014. "Cutfem: discretizing geometry and partial differential equations". *International Journal for Numerical Methods in Engineering*.

[51] Moës, N., Dolbow, J., and Belytschko, T., 1999. "A finite element method for crack growth without remeshing". *International Journal for Numerical Methods in Engineering,* ***46***(1), pp. 131–150.

[52] Simone, A., Duarte, C., and Van der Giessen, E., 2006. "A generalized finite element method for polycrystals with discontinuous grain boundaries". *International Journal for Numerical Methods in Engineering,* ***67***(8), pp. 1122–1145.

[53] Soghrati, S., 2014. "Hierarchical interface-enriched finite element method: An automated technique for mesh-independent simulations". *Journal of Computational Physics,* ***275***, pp. 41–52.

[54] Soghrati, S., and Ahmadian, H., 2015. "3D hierarchical interface-enriched finite element method: Implementation and applications". *Journal of Computational Physics,* ***299***, pp. 45–55.

[55] Soghrati, S., Nagarajan, A., and Liang, B., 2017. "Conforming to Interface structured adaptive mesh refinement technique for modeling heterogeneous materials". *Computational Mechanics,* ***125***, pp. 24–40.

[56] Soghrati, S., Xiao, F., and Nagarajan, A., 2017. "A conforming to interface structured adaptive mesh refinement technique for modeling fracture problems". *Computational Mechanics,* ***59***(4), pp. 667–684.

[57] Nagarajan, A., and Soghrati, S., 2018. "Conforming to interface structured adaptive mesh refinement: 3D algorithm and implementation". *Computational Mechanics*, pp. 1–26.

[58] Ahmadian, H., Liang, B., and Soghrati, S., 2017. "An integrated computational framework for simulating the failure response of carbon fiber reinforced polymer composites". *Computational Mechanics,* ***60***(6), Dec, pp. 1033–1055.

[59] Liang, B., Nagarajan, A., Hudoba, M. W., Alvarez, R., Castro, C. E., and Soghrati, S., 2017. "Automated quantification of the impact of defects on the mechanical behavior of deoxyribonucleic acid origami nanoplates". *Journal of biomechanical engineering,* ***139***(4), p. 041003.

[60] Abedi, R., Haber, R. B., and Petracovici, B., 2006. "A spacetime discontinuous Galerkin method for elastodynamics with element-level balance of linear momentum". *Computer Methods in Applied Mechanics and Engineering,* ***195***, pp. 3247–73.

[61] Zhou, H., Feng, Q., Kan, Y., Gao, L., and Dong, S., 2013. "ZrB2-SiC coatings prepared by vapor and liquid silicon in-

filtration methods: Microstructure and oxidation resistance property". *Journal of Inorganic Materials,* ***28***(10).

[62] Acton, K. A., Baxter, S. C., Bahmani, B., Clarke, P. L., and Abedi, R., 2018. "Voronoi tessellation based statistical volume element characterization for use in fracture modeling". *Computer Methods in Applied Mechanics and Engineering,* ***336***, pp. 135–155.

[63] Nguyen, V. P., Lloberas-Valls, O., Stroeven, M., and Sluys, L. J., 2011. "Homogenization-based multiscale crack modelling: From micro-diffusive damage to macro-cracks". *Computer Methods in Applied Mechanics and Engineering,* ***200***(9), pp. 1220–36.

[64] Daphalapurkar, N., Ramesh, K., Graham-Brady, L., and Molinari, J., 2011. "Predicting variability in the dynamic failure strength of brittle materials considering pre-existing flaws". *Journal of the Mechanics and Physics of Solids,* ***59***(2), pp. 297–319.

[65] Ostoja-Starzewski, M., 1998. "Random field models of heterogeneous materials". *International Journal of Solids and Structures,* ***35***(19), pp. 2429–2455.

[66] Bazant, Z. P., and Planas, J., 1997. *Fracture and size effect in concrete and other quasibrittle materials*, Vol. 16. CRC press.

[67] Ranganathan, S. I., and Ostoja-Starzewski, M., 2008. "Universal elastic anisotropy index". *Physical Review Letters,* ***101***(5), p. 055504.

[68] Camacho, G. T., and Ortiz, M., 1996. "Computational modelling of impact damage in brittle materials". *International Journal of Solids and Structures,* ***33***, pp. 2899–2938.

[69] Abedi, R., Haber, R. B., Thite, S., and Erickson, J., 2006. "An *h*–adaptive spacetime–discontinuous Galerkin method for linearized elastodynamics". *European Journal of Computational Mechanics,* ***15***(6), pp. 619–42.

[70] Abedi, R., Hawker, M. A., Haber, R. B., and Matouš, K., 2009. "An adaptive spacetime discontinuous Galerkin method for cohesive models of elastodynamic fracture". *International Journal for Numerical Methods in Engineering,* ***1***, pp. 1–42.

[71] Omidi, O., Abedi, R., and Enayatpour, S., 2015. "An adaptive meshing approach to capture hydraulic fracturing". In The 49th US Rock Mechanics/Geomechanics Symposium. ARMA 15-572.